MNRAS **000**, 000–000 (0000) Preprint 9 November 2016 Compiled using MNRAS LATEX style file v3.0

The asteroseismic surface effect from a grid of 3D convection simulations. I. Frequency shifts from convective expansion of stellar atmospheres

Regner Trampedach[1,2⋆], Magnus J. Aarslev[2], Günter Houdek[2], Remo Collet[2], Jørgen Christensen-Dalsgaard[1], Robert F. Stein[3] and Martin Asplund[4]
[1] *Space Science Institute, 4750 Walnut Street, Suite 205, Boulder, CO 80301 USA*
[2] *Stellar Astrophysics Centre, Dept. of Physics and Astronomy, Ny Munkegade 120, Aarhus University, DK–8000 Aarhus C, Denmark*
[3] *Department of Physics and Astronomy, Michigan State University East Lansing, MI 48824, USA*
[4] *Research School of Astronomy and Astrophysics, Mt. Stromlo Observatory, Cotter Road, Weston ACT 2611, Australia*

Received 9 November 2016/ Accepted 9 November 2016

arXiv:1611.02638v1 [astro-ph.SR] 8 Nov 2016

ABSTRACT

We analyse the effect on adiabatic stellar oscillation frequencies of replacing the near-surface layers in 1D stellar structure models with averaged 3D stellar surface convection simulations. The main difference is an expansion of the atmosphere by 3D convection, expected to explain a major part of the asteroseismic surface effect; a systematic overestimation of p-mode frequencies due to inadequate surface physics.

We employ pairs of 1D stellar envelope models and 3D simulations from a previous calibration of the mixing-length parameter, α. That calibration constitutes the hitherto most consistent matching of 1D models to 3D simulations, ensuring that their differences are not spurious, but entirely due to the 3D nature of convection. The resulting frequency shift is identified as the *structural* part of the surface effect. The important, typically non-adiabatic, *modal* components of the surface effect are not included in the present analysis, but relegated to future papers.

Evaluating the structural surface effect at the frequency of maximum mode amplitude, $\nu_{\rm max}$, we find shifts from $\delta\nu = -0.8\,\mu$Hz for giants at $\log g = 2.2$ to $-35\,\mu$Hz for a ($T_{\rm eff} = 6901\,$K, $\log g = 4.29$) dwarf. The fractional effect $\delta\nu(\nu_{\rm max})/\nu_{\rm max}$, ranges from -0.1% for a cool dwarf (4185 K, 4.74) to -6% for a warm giant (4962 K, 2.20).

Key words: Stars: atmospheres – stars: evolution – convection

1 INTRODUCTION

The asteroseismic surface effect is a systematic difference between measured stellar p-mode frequencies and theoretical, adiabatic frequencies of stellar models, known to arise from differences in the surface layers (Brown 1984; Christensen-Dalsgaard, Däppen & Lebreton 1988).

Rosenthal et al. (1999) first analysed the helioseismic surface effect in terms of frequency differences between 1D models and averaged 3D surface simulations. They concluded that most of the effect is due to a convective expansion of the atmosphere, compared to 1D convective atmospheres. Similar analyses have now been carried out by Piau et al. (2014) and Magic & Weiss (2016) for the Sun, Sonoi et al. (2015) for a grid of 10 simulations, and by Ball et al. (2016) for four simulations on the main sequence, all for solar metallicity.

Houdek et al. (2017) recently presented an analysis of various components of the surface effect for the solar case. We use the same 3D solar simulation, but extend our analysis to the whole grid of solar metallicity simulations (Trampedach et al. 2013), to explore the behaviour with atmospheric parameters. On the other hand, we limit our analysis to only include the stratification contributions to the seismic surface effect (see Section 3), and defer the evaluation of modal components to a future paper.

2 THE 3D CONVECTIVE ATMOSPHERE SIMULATIONS

We use the grid of 37 fully compressible 3D radiation-coupled hydrodynamic simulations of stellar surface convection by Trampedach et al. (2013). The grid covers effective temperatures, $T_{\rm eff} = 4\,200$–$6\,900\,$K on the main sequence, and $T_{\rm eff} = 4\,300$–$5\,000\,$K and $\log g = 2.2$–2.4 for giants, all

⋆ E-mail: rtrampedach@SpaceScience.org

© 0000 The Authors

for solar metallicity. The simulations evolve the conservation equations of mass, momentum and energy in a small box straddling the stellar photosphere extending up to a logarithmic, Rosseland optical depth of $\log\tau = -4.5$ and reaching more than 6 pressure scale heights below the photosphere. This is deep enough that they can be safely merged with 1D models below, i.e., the convective fluctuations there are small, as is the deviation from an adiabatic stratification.

The simulations employ a 15 element custom calculation of the so-called Mihalas-Hummer-Däppen equation of state (EOS) (Hummer & Mihalas 1988), and realistic monochromatic opacities (Trampedach et al. 2014a). An open bottom boundary mimics the effect of the large entropy reservoir of the convection zone below the simulation, ensuring a realistic entropy contrast inside the simulations.

2.1 Consistently patched 1D models and 3D simulations

The above simulations were previously used to calibrate the main parameter, α, of the mixing-length formulation (MLT) of 1D convection (Trampedach et al. 2014b). This was carried out as a matching of temperature and density at the common total pressure of the matching point. The matching point is chosen as deep in the simulation as possible (less than a pressure scale-height from the bottom), while still avoiding boundary effects (See Fig. 1). The 1D models include a turbulent pressure (See Sect. 3.1), $p_{\rm t}^{\rm 1D} = \beta\varrho v_{\rm MLT}^2$, with form-factor β. This pressure is smoothly suppressed towards the surface, as the MLT version would give an unphysically sharply peaked $p_{\rm t}^{\rm 1D}$. The approach is therefore to include it at the fitting point and below, to ensure a consistent match to the 3D simulations, as shown in Fig. 1, but suppress it before it becomes important for the hydrostatic equilibrium (see Trampedach et al. 2014b, for details). Formulating a realistic turbulent pressure for 1D models is a separate project. We iterated for α and β until both converged to within 10^{-6} resulting in deviations of $\log T$ and $\log\varrho$ at the matching point of less than 10^{-5} and 10^{-3}, respectively. The 1D models employ the exact same EOS and abundances as the simulations, and in the atmosphere use the opacities of the simulations, and the temperature stratification, $T(\tau)$, extracted from the simulations (Trampedach et al. 2014a). This ensures that the 1D envelope model and the averaged 3D simulation can be patched together for a continuous and smooth model across the matching point. This is illustrated in Fig. 1 for the warmest dwarf simulation, which deviates most strongly from its calibrated 1D model.

The 3D simulations are slightly more extended than the (un-patched) 1D models (giving rise to the structural surface effect), and hence have slightly lower $T_{\rm eff}$ and $\log g$, corresponding to their common mass and luminosity. The simulations are carried out in the plane-parallel approximation (constant surface gravity) and the averages are therefore corrected for sphericity consistent with the radius of the 1D model, to avoid glitches at the matching point. Of these steps, only the consistent EOS and abundances have been implemented in previous work (Piau et al. 2014; Sonoi et al. 2015; Ball et al. 2016; Magic & Weiss 2016).

The 1D models are computed with the stellar envelope code by Christensen-Dalsgaard & Frandsen (1983), which is closely related to the ASTEC stellar structure and evolution code (Christensen-Dalsgaard 2008a). Being envelope models, they ignore the innermost 5% of the star, as well as nuclear reactions and any other composition-altering processes. The limited extent constrains the modes available for our analysis to those with turning points well inside the envelope model. Our results will, however, not be affected, as the surface effect is indeed confined close to the surface and fully contained even in the 3D, deep atmosphere simulations.

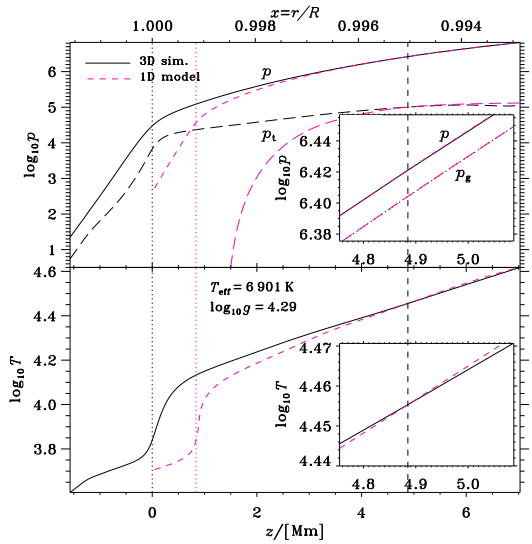

Figure 1. Top panel: the pressures (black) of the 3D simulation (also shown in Fig. 2) and the calibrated 1D model (magenta). The insert panel is a zoom around the matching point (vertical, black dashed, shared with main panel). The surface (where $\langle T\rangle = T_{\rm eff}$) is shown for the 3D simulation (vertical, black dotted) and the 1D model (magenta dotted), The difference causes the structural surface effect. Bottom panel: Same as top panel but for the logarithmic temperature.

3 THE STRUCTURAL PART OF THE ASTEROSEISMIC SURFACE EFFECT

We compare adiabatic mode frequencies from two cases:
UPM: pure 1D models calibrated against the 3D simulations as detailed in Section 2.1 (un-patched models), and
PM: those same 1D models, but with the surface layers substituted by the averaged 3D simulations (patched models).
The two models are by construction identical interior to the 3D simulations. The frequency differences between PM and UPM will be the asteroseismic surface effect due to convective effects on the average stratification of the atmospheres. This is in contrast to effects from the mode dynamics through direct interactions between 3D convection and modes. We refer to these two classes of seismic surface effects as *structure effects* and *modal effects*, respectively.

The modal effects include the response to the pulsations of turbulent pressure and non-adiabatic energetics, including the convective flux. Houdek et al. (2017) computed modal components for the solar case, based on a non-local, time-dependent mixing-length formulation of convection (Gough 1977), and found them to be of the opposite sign and about 30% of the structure effects, bringing the total into remark-

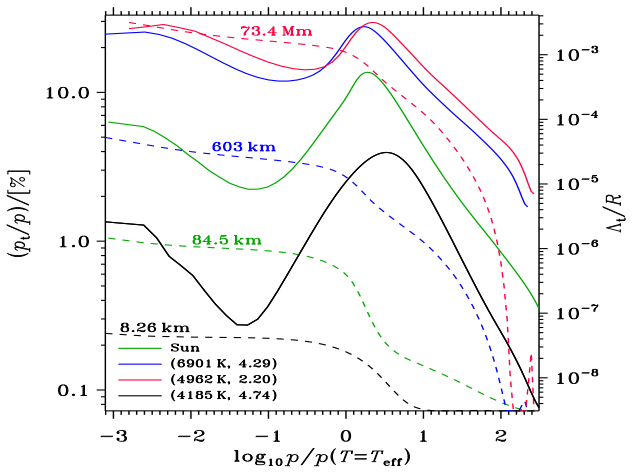

Figure 2. Ratios of turbulent to total pressures (solid lines, left-hand scale) for four simulations, spanning the range of behaviours in the grid of simulations, with $T_{\rm eff}$ and $\log g$ indicated in parenthesis. The right-hand axis shows the atmospheric expansion due to the turbulent pressure only, $\Lambda_{\rm t}$ (dashed lines), as fraction of stellar radius. The total $\Lambda_{\rm t}$ is indicated for each curve.

able agreement with observations. Using just the structural effects, as presented here, will therefore give frequency shifts that are larger than the total seismic surface effect (assuming that modal effects are always positive). Computing modal components directly from the 3D simulations is a significant project and will be the subject of future papers. The structure effect itself has two components, as detailed below.

3.1 Turbulent pressure contribution

The horizontally and temporally averaged (denoted by $\langle \ldots \rangle$) turbulent pressure

$$p_{\rm t} = \langle \varrho u_z^2 \rangle \ , \quad \text{with} \quad p = \langle p_{\rm g} \rangle + p_{\rm t} \ , \tag{1}$$

contributes about half of the total convective expansion, where ϱ is the density, u_z is the vertical velocity, $p_{\rm g}$ is the gas pressure and p the total pressure. This expansion, $\Lambda_{\rm t}$, by $p_{\rm t}$ can be directly quantified by integrating hydrostatic equilibrium over just that component of the pressure

$$\frac{{\rm d}p}{{\rm d}z} = g\langle\varrho\rangle \quad \Leftrightarrow \quad \Lambda_{\rm t} \equiv \Delta z_{\rm t} = \int \frac{{\rm d}p_{\rm t}}{g\langle\varrho\rangle} \ , \tag{2}$$

where z is the depth in the atmosphere. This $\Lambda_{\rm t}$ is exact in the sense that ϱ, T and $p_{\rm g}$ do not change with $p_{\rm t}$, only the location where those values occur are shifted. The turbulent contribution to the total pressure, $p_{\rm t}/p$, peaks at between 4% for the coolest dwarf in our grid, and 30% for our warmest giant (see Fig. 2), just below the top of the convection zone.

The upturn in $p_{\rm t}/p$ above the photosphere, is not convective but rather the effect of travelling waves escaping the acoustic cavity above the acoustic cut-off frequency. Notice that in local MLT formulations of convection, the convective velocities would drop to zero from the peak of the $p_{\rm t}/p$-ratio in a small fraction of a pressure scale-height, missing about half of the atmospheric expansion from turbulent pressure.

3.2 Convective backwarming

Another, less straightforward, contribution to the convective expansion of the atmosphere is caused by convective fluctuations in the opacity. Since the top of convective envelopes occurs at temperatures and densities where the opacity, κ, is extremely sensitive to temperature (about $\kappa \propto T^9$ for the Sun) the convective temperature fluctuations will cause much larger fluctuations in opacity. The warm upflows will be shielded from cooling until (geometrically) close to the photosphere, as the high opacity constitutes a geometric compression of the optical depth scale. This effectively causes a warming below the photosphere, compared to a model based on the opacity of the average stratification. The high power in T means the opposing cooling effect in the downdrafts will be smaller. The upflows also occupy a larger fractional area. Coupled with the non-linear nature of radiative transfer, the cooler downdrafts do not cancel the effect in the upflows, resulting in a net warming below the photosphere. This in turn gives a larger pressure scale-height and hence an expansion of the atmosphere, denoted Λ_κ. The effect has a similar magnitude as that from the turbulent pressure. The two effects are also correlated, as the amplitude of convective velocities and temperature fluctuations are correlated. The total convective expansion by the two mechanisms is denoted Λ and is shown in Fig. 5 of Trampedach et al. (2013). We compute this as the radial off-set of pressure stratifications between the PM and UPM models, high in the atmosphere.

3.3 Excluding the modal response of $p_{\rm t}$

Rosenthal et al. (1999) considered the effect of $p_{\rm t}$ on modes using two simple cases as illustrative examples:
a): $p_{\rm t}$ reacts exactly as $p_{\rm g}$, i.e., is in phase with the density fluctuations and proportional to them by γ_1.
b): $p_{\rm t}$ has a completely incoherent response to modal density fluctuations, and over time has no net effect on mode frequencies or eigen-functions, i.e., exhibits no modal response. Case b) result in Lagrangian pressure fluctuations $\delta \ln p = (0 \cdot p_{\rm t}/p + \gamma_1 p_{\rm g}/p)\, \delta \ln \varrho$, where γ_1 is the adiabatic exponent of the gas, and the parenthesis is referred to as the *reduced* γ_1. This should not be viewed as a reduction of the thermodynamic quantity, but rather a statement about the turbulent pressure response to modes. Previous calculations (e.g., Piau et al. 2014; Sonoi et al. 2015; Ball et al. 2016; Magic & Weiss 2016) have all used case a), which is both an unjustified choice of the modal response to $p_{\rm t}$, as well as an incomplete accounting of modal components.

To isolate the structural surface effect, we shall here use case b), as did Houdek et al. (2017), to assume that there is no modal response to $p_{\rm t}$, This results in a structural part of the surface effect which, for the solar case, is about 1.4 times larger than the total surface effect at the acoustic cut-off frequency, and about 3 times larger at $\nu_{\rm max}$ (see Houdek et al. 2017).

4 FREQUENCY SHIFTS AND DISCUSSION

We analyse the differences between adiabatic frequencies (computed with ADIPLS; Christensen-Dalsgaard 2008b) for

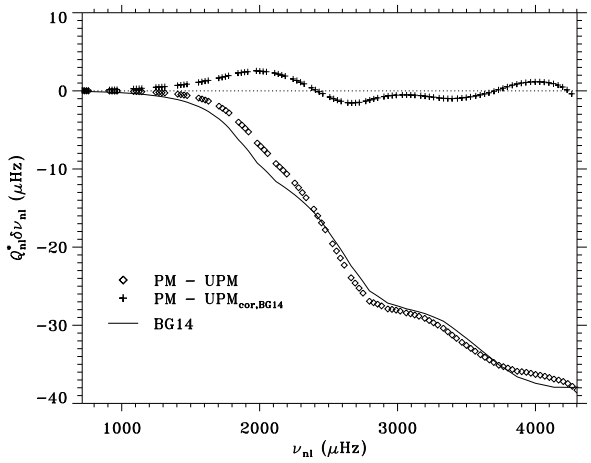

Figure 3. Scaled frequency differences in the sense: patched minus un-patched models (Sect. 3) shown with ⋄, for $T_{\rm eff} = 6\,569$ K and $\log g = 4.45$. We show both the two-term, BG14-fit (solid line), and the residual of that fit (+).

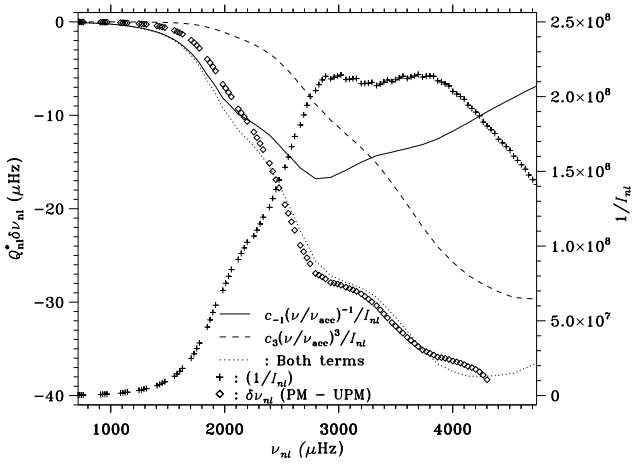

Figure 4. The various contributions to the fit to Eq. (3), for the case shown in Figure 3. The ν^{-1}-term (solid) and the ν^3-term (dashed), and the total fit (dotted) is compared to the actual frequency shift (⋄). The inverse mode inertia (+) is also shown.

the patched and unpatched models, which we identify as the surface effect due to differences in the average atmospheric structure of the two cases. We do this for modes with degree $l = 20$–23 and all orders, n, that have frequencies, ν_{nl}, below the acoustic cut-off frequency, $\nu_{\rm ac}$. This l-range ensures the modes are confined well within the envelope models.

As first suggested by Ball & Gizon (2014, BG14), we fit the frequency differences, $\delta\nu_{nl}$, to expressions of the form

$$I_{nl}\delta\nu_{nl} = c_{-1}\left(\nu/\nu_{\rm ac}\right)^{-1} + c_3\left(\nu/\nu_{\rm ac}\right)^3 \ , \qquad (3)$$

where we evaluate the acoustic cut-off frequency as

$$\nu_{\rm ac} = 5\,100\,\mu{\rm Hz}\,(g/g_\odot)\sqrt{T_{{\rm eff}\odot}/T_{\rm eff}} \ , \qquad (4)$$

scaled by the solar value (Jiménez 2006). Equation (3) was motivated by Gough (1990), exploring the origins of the solar-cycle modulation of frequencies. He found that a change of scale-height in the superadiabatic layer would give rise to the first term, while the ν^3-term arises from a change to the sound speed that keeps the density unchanged. In terms of the convective expansion, these would arise from the convective backwarming and the turbulent pressure, respectively.

The frequency shifts in Eq. (3) are scaled by the mode inertia, I_{nl} (e.g., Aerts, Christensen-Dalsgaard & Kurtz 2010). This scaling renders the frequency shifts independent of l, and likewise for the fit (to within 0.25%). This confirms that the restrictions on l, from using envelope models, do not limit the validity of our results. Rather, it is an improvement, since a particular atmosphere simulation can correspond to several interior models, in different stages of evolution, potentially affecting the mode inertia. Our procedure effectively separates the surface part, c_{-1} and c_3, from the interior part, I_{nl} (supplied by the user), of $\delta\nu_{nl}$.

In Figures 3–6, the frequency shifts are reduced to $l = 20$ by scaling with $Q_{nl}^{*} = I_{nl}/I_{20}(\nu_{nl})$, where I_{20} is I_{n20} interpolated to ν_{nl}. An example of our fit to Eq. (3) is shown in Fig. 3 for a warm dwarf. A power-law fit (Kjeldsen, Bedding & Christensen-Dalsgaard 2008) is obviously unable to fit the frequency differences in Fig. 3 over the full frequency range, as discussed by Sonoi et al. (2015).

How the two terms and the mode inertia contribute to the BG14-fit, is shown in Figure 4. It is apparent that the various bumps in the frequency shift are due to the mode inertia, and the main reason the BG14 fit is so successful.

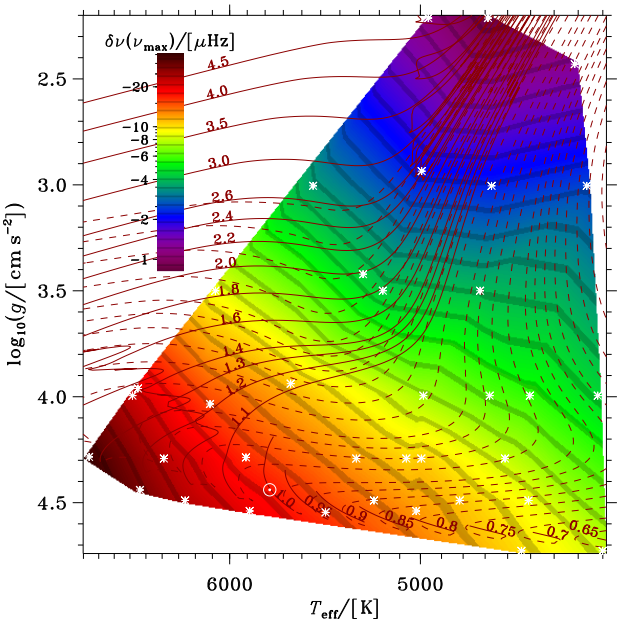

Figure 5. The amplitude of the frequency shift (patched minus unpatched) at $\nu_{\rm max}$, as function of $T_{\rm eff}$ and $\log g$. The colour-scale is logarithmic. The location of the solar (⊙) and stellar (∗) simulations are indicated in white. MESA (Paxton et al. 2011) stellar evolution tracks are over-plotted for masses as indicated. The dashed part shows the pre-main-sequence contraction.

The amplitude of the surface effect at the frequency of maximum power, estimated as $\nu_{\rm max} \simeq 0.6\nu_{\rm ac}$, is shown in Figure 5. This qualitatively agrees with analysis of *Kepler* observations (Metcalfe et al. 2014) of 42 F–G dwarfs and sub-giants. We performed linear regression of their surface effects at $\nu_{\rm max}$, and of ours interpolated to their targets, giving similar increases with $\log T_{\rm eff}$ and $\log g$. Our amplitudes are 2–8 times larger, however, partly due to our omission of

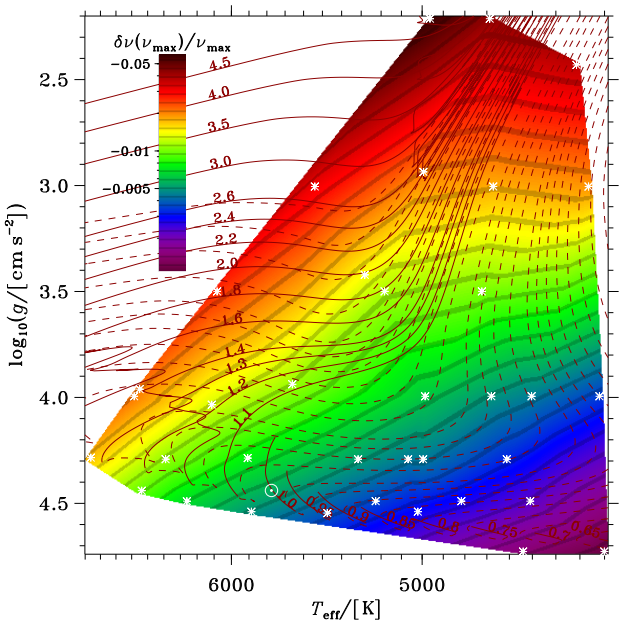

Figure 6. As Fig. 5, except the amplitude is normalised by $\nu_{\max}$, to highlight the relative significance of the surface effect.

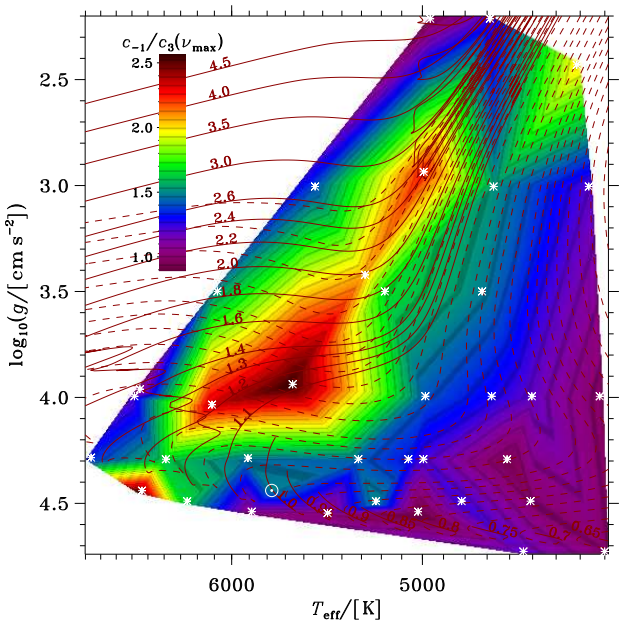

Figure 7. As Fig. 5, but showing the ratio of the two terms of Eq. [3]) at $\nu_{\max}$, $(c_{-1}/c_3)\cdot(\nu_{\max}/\nu_{\rm ac})^{-4}$.

modal effects, expected to result in a surface effect larger than the total. Another important factor is how stellar fits to seismic observations often exhibit coupled parameters. In particular the surface effect, mixing length and helium content can be strongly correlated, stressing the importance of constraining these quantities independently.

Fig. 5 shows that the magnitude of the surface effect increases roughly as g. To take out this variation and highlight the relative importance of the effect we show in Figure 6 the fractional surface effect, in units of $\nu_{\max}$. This is seen to be predominantly, but not exclusively, a function of the atmospheric expansion, based on the near proportionality between Figure 6 and Figure 5 of Trampedach et al. (2013). The ratio of the two terms in Eq. (3) at $\nu_{\max}$, is shown in Figure 7, and illustrates a general change of shape with atmospheric parameters. The c_{-1}-term dominates along a ridge running parallel with the warm edge of our grid.

We have evaluated the stuctural part of the asteroseismic surface effect, as the effect on frequencies of the atmospheric expansion by realistic 3D convection, relative to 1D MLT stellar models. Contrary to recent studies, we isolate the structural part from the modal part of the surface effect by ignoring the turbulent pressure response to modes, through the use of the so-called reduced γ_1. For the solar case, this gives a frequency shift that is larger than the total, as the modal part turns out to have the opposite sign. Our results are well fit by BG14's expression, which also eliminates first-order dependencies on l, so we can benefit from using envelope models instead of full evolution models.

ACKNOWLEDGEMENTS

We thank the referee for helpful comments. RT acknowledges funding from NASA grant NNX15AB24G. Funding for the Stellar Astrophysics Centre is provided by The Danish National Research Foundation (Grant DNRF106).

REFERENCES

Aerts C., Christensen-Dalsgaard J., Kurtz D. W., 2010, Asteroseismology, 1st edn., Astron. & Astroph. Library. Springer, Dordrecht
Ball W. H., Beeck B., Cameron R. H., Gizon L., 2016, A&A, 592, A159
Ball W. H., Gizon L., 2014, A&A, 568, A123
Brown T. M., 1984, Science, 226, 687
Christensen-Dalsgaard J., 2008a, Ap&SS, 316, 13
Christensen-Dalsgaard J., 2008b, Ap&SS, 316, 113
Christensen-Dalsgaard J., Däppen W., Lebreton Y., 1988, Nature, 336, 634
Christensen-Dalsgaard J., Frandsen S., 1983, Sol. Phys., 82, 469
Gough D. O., 1977, ApJ, 214, 196
Gough D. O., 1990, in Lecture Notes in Physics, Vol. 367, Progress of Seismology of the Sun and Stars, Osaki Y., Shibahashi H., eds., Springer, Berlin, 283
Houdek G., Trampedach R., Aarslev M. J., Christensen-Dalsgaard J., 2017, MNRAS, 464, L124
Hummer D. G., Mihalas D., 1988, ApJ, 331, 794
Jiménez A., 2006, ApJ, 646, 1398
Kjeldsen H., Bedding T. R., Christensen-Dalsgaard J., 2008, ApJ, 683, L175
Magic Z., Weiss A., 2016, A&A, 592, A24
Metcalfe T. S. et al., 2014, ApJS, 214, 27
Paxton B., Bildsten L., Dotter A., Herwig F., Lesaffre P., Timmes F., 2011, ApJS, 192, 3
Piau L., Collet R., Stein R. F., Trampedach R., Morel P., Turck-Chièze S., 2014, MNRAS, 437, 164
Rosenthal C. S., Christensen-Dalsgaard J., Nordlund Å., Stein R. F., Trampedach R., 1999, A&A, 351, 689
Sonoi T., Samadi R., Belkacem K., Ludwig H.-G., Caffau E., Mosser B., 2015, A&A, 583
Trampedach R., Asplund M., Collet R., Nordlund Å., Stein R. F., 2013, ApJ, 769, 18
Trampedach R., Christensen-Dalsgaard J., Nordlund Å., Asplund M., Stein R. F., 2014a, MNRAS, 442, 805
Trampedach R., Christensen-Dalsgaard J., Nordlund Å., Asplund M., Stein R. F., 2014b, MNRAS, 445, 4366